Characterization of a Volumetric Metamaterial Realization of an Artificial Magnetic Conductor for Antenna Applications

Aycan Erentok, *Student Member, IEEE*, Paul L. Luljak, *Student Member, IEEE*, and
Richard W. Ziolkowski, *Fellow, IEEE*

Abstract—The design, fabrication and measurement of a volumetric metamaterial realization of an artificial magnetic conductor (AMC) is presented. In contrast to most current realizations of AMCs, such as the mushroom and the uniplanar compact photonic bandgap surfaces, the present design has no perfect electric conductor ground plane. The perfect magnetic conductor properties were designed with capacitively loaded loops for *X* band operation at 10 GHz. Very good agreement between the numerical and experimental scattering results was achieved. The performance of a dipole antenna radiating in the presence of this volumetric metamaterial AMC is quantified numerically. Resonant interactions of the antenna and metamaterial structure lead to a significant enhancement of the radiated field amplitudes and isolation measured as the front-to-back ratio.

Index Terms—Antennas, artificial dielectrics, artificial magnetic conductor (AMC), metamaterials, scattering.

I. INTRODUCTION

IN RECENT years, there has been a renewed interest in using sub-wavelength structures to develop materials that mimic known material responses or that qualitatively have new response functions that do not occur in nature. These metamaterial efforts have included a number of periodic ground plane structures to realize artificial magnetic conductors (AMCs) for a variety of antenna applications. The mushroom realization, first introduced by Sievenpiper *et al.*, [1]–[4], has been very successful and have led to a number of commercial applications. It consists of a ground plane separated (by a dielectric) from a plane of periodically located elements (essentially a frequency selective surface (FSS) layer), each of which is connected to the ground plane by a via. Square and hexagonal shaped elements are common, but more exotic shaped elements have been used. Its AMC behavior results from the formation of a periodic set of small, parallel resonant *LC* circuits. The spacing between the edges of the elements controls the capacitance, and the magnetic flux created between the patches and the ground plane defines the inductance. A second popular AMC realization is the uniplanar compact photonic bandgap (UC-PBG) structure,

first introduced by T. Itoh *et al.*, [5]–[8]. The UC-PBG structures again consist of a ground plane separated (by a dielectric) from a plane of periodically located conducting elements, i.e., the resulting structure is basically an FSS layer over a dielectric loaded ground plane. In contrast to the mushroom surface, the UC-PBG structures realize the AMC properties without vias but with more complex element shapes. The UC-PBG structures lend themselves to easier fabrication approaches using standard etching techniques. The UC-PBG structures have been utilized for both antenna, microwave circuit and waveguide-wall applications.

In this paper we introduce an AMC slab designed to operate in the *X* band at 10 GHz that does not require a ground plane. The capacitively-loaded loop (CLL) elements considered here are simplifications of the split ring resonators (SRRs) used successfully in several double negative (DNG) metamaterials (metamaterials with $\varepsilon < 0$ and $\mu < 0$) realizations [9]–[12] and of the C-particles used successfully for a radar signature reduction application [13]. Variations of these elements have been used successfully in DNG metamaterial transmission line studies [14]. The reflection properties of the CLL-based AMC slab are obtained for several configurations. The $\pm 45°$ bandwidth was obtained in all cases to provide some expectation of success for the CLL-based AMC slab for an actual antenna application. As noted in [15]–[17], the zero phase crossing point may not be the optimal operating point for such an application.

Consider a normally incident plane wave that scatters from a semi-infinite dielectric-magnetic slab of depth d embedded in free-space. If the permittivity and permeability of the slab are ε and μ, the corresponding impedance and the wave number are, respectively, $\eta = \sqrt{\mu/\varepsilon}$ and $k = \omega\sqrt{\varepsilon}\sqrt{\mu}$. The free-space values of these parameters are $\varepsilon_0, \mu_0, \eta_0 = \sqrt{\mu_0/\varepsilon_0}$, and $k_0 = \omega\sqrt{\varepsilon_0}\sqrt{\mu_0}$. The relative permittivity and permeability are given by the expressions $\varepsilon = \varepsilon_r\varepsilon_0$ and $\mu = \mu_r\mu_0$. The reflection, S_{11}, and transmission, S_{21}, values are easily obtained using Maxwell's equations and are given by the expressions

$$S_{11} = \frac{\eta - \eta_0}{\eta + \eta_0} \frac{1 - e^{-j2kd}}{1 - \left(\frac{\eta-\eta_0}{\eta+\eta_0}\right)^2 e^{-j2kd}} \qquad (1)$$

$$S_{21} = \frac{4\eta\eta_0}{(\eta + \eta_0)^2} \frac{e^{-jkd}}{1 - \left(\frac{\eta-\eta_0}{\eta+\eta_0}\right)^2 e^{-j2kd}}. \qquad (2)$$

The class of metamaterials under consideration have been shown to exhibit very large wave impedances, i.e.,

$\eta = \sqrt{\mu/\varepsilon} \to \infty$. Consequently, the reflection and transmission coefficient values become

$$\lim_{|\eta| \to \infty} S_{11} = +1$$
$$\lim_{|\eta| \to \infty} S_{21} = 0. \qquad (3)$$

Thus, a slab exhibiting a large impedance, i.e., a high-Z slab, will act as a broad bandwidth in-phase reflector, i.e., as an AMC. The reflection and transmission values in (3) for such a high-Z slab are recovered for any (nontrivially) finite-sized slab. If, however, the permeability is not extremely large, the wave impedance can still be made to be extremely large if the permittivity is near zero. This would mean that the index of refraction $n = \sqrt{\varepsilon/\varepsilon_0}\sqrt{\mu/\mu_0}$ would become small as the impedance became large. Consequently, a high-Z/low-n slab would also act as an AMC. Finally, we note that for a slab terminated with a PEC, the reflection coefficient relative to the input face of the slab is

$$S_{11} = \frac{\frac{\eta - \eta_0}{\eta + \eta_0} - e^{-j2kd}}{1 - \frac{\eta - \eta_0}{\eta + \eta_0} e^{-j2kd}} \qquad (4)$$

and also gives the same limits when the magnitude of the impedance is large, e.g.

$$\lim_{|\eta| \to \infty} S_{11} = +1. \qquad (5)$$

While an infinite PEC-grounded slab guarantees a complete reflection, a finite PEC-grounded structure in a realistic situation introduces a number of complications for antenna applications. The anticipated benefits of an AMC slab without a ground plane in an antenna application include the absence of the associated image and scattering-induced currents on the back side of a finite ground plane, a lowered probability of surface waves, and lighter weight. Without the additional image and scattering-induced currents, radiation in the back direction should be significantly reduced. Moreover, despite the intent for the additional structures over the ground plane to prevent the images sources from shorting out the antenna, they can still be problematic when the antenna is extremely close to a PEC-backed structure. The absence of a ground plane removes many of these issues.

Thus, a low-n/high-Z slab without a PEC ground plane would appear to be a very desirable goal for artificial magnetic conductors in application purposes, particularly those associated with antennas. It will be demonstrated that the volumetric CLL-based AMC slab exhibits these low-n/high-Z properties. However, we note that since the CLL elements under consideration are very resonant, we expect that the metamaterial CLL-based slab will exhibit AMC properties only in a narrow band of frequencies. Clearly, if one could design a broad bandwidth metamaterial element that exhibited the high-Z/low-n properties over a large frequency range, it would be the most desirable.

Since an important reason why the use of in-phase reflectors is to enhance the performance of compact, low profile radiating systems, the behavior of a dipole antenna in the presence of the realized volumetric CLL-based AMC block is quantified numerically. Several dipole antenna sizes are considered.

It will be shown that a resonance can be established between the dipole antenna and the CLL-based AMC block by varying the distance between them. If the free space wavelength of driving source is λ_0, these resonant distances were found to be $\lambda_0/15$ or smaller. The block itself, however, is rather small, its face toward the dipole being $0.18\lambda_0$ wide and $0.85\lambda_0$ in height. Thus, the strength of the response is dependent on the size of the dipole. For a half-wave dipole, which is almost as tall as the block, slightly more than a 1.22-fold enhancement of the reflected field is realized at the resonance. On the other hand, a 6.26-fold enhancement is obtained for a small $0.08\lambda_0$ dipole. For a $0.325\lambda_0$ dipole, whose size fits the block naturally, a 2.29-fold enhancement is realized. Moreover, in this case a null in the direction antipodal to that of the peak field value is formed at the resonance distance and the corresponding front-to-back ratio is significant—approximately a 44 dB value. The near field distributions exhibit similar enhanced characteristics as well. The E plane and H plane patterns of this dipole and the volumetric CLL-based AMC block system are also obtained. Because of the small size of the block, these patterns are broad in the hemisphere containing the dipole with little field being radiated into the back hemisphere. However, if one would like to enhance the directivity of this system, the size of the block would have to be increased to allow for some sort of additional texturing of its surface to achieve soft or hard surface effects or for the insertion of additional structures to achieve electromagnetic bandgap effects. In that manner one could use many of the ideas reported in this special issue to redirect some of the side and back-directed field energy in the E or H plane toward the broadside direction.

The CLL-based AMC slabs and blocks presented below were designed with ANSOFT's High Frequency Structure Simulator (HFSS), version 9.1. The details of the design simulations will be discussed in Section II. The element fabrication will be described in Section III. The experimental set-up and measurements will be discussed in Section IV. Very good agreement between the design and experimental results was obtained. The numerical simulations describing the interaction of the dipole antenna with the CLL-based AMC block are presented in Section V. Conclusions and future efforts will be given in Section VI.

II. HFSS Simulation Results

The DNG metamaterial components are derived from those successfully tested in [12]. There, an integrated set of negative permittivity (capacitively loaded strip [CLS]) and negative permeability [SRR] elements were used to obtain a negative index of refraction block that was matched to free space at *X* band frequencies. The metamaterial elements considered here consist only of capacitively loaded loops (CLLs). These CLLs behave similarly to the SRRs but greatly simplify fabrication issues. These elements were designed to be embedded in Rogers 5880 Duroid, a low loss dielectric characterized by the parameters $\varepsilon_r = 2.2$, $\mu_r = 1.0$, and $\tan\phi_{\text{loss}} = 0.0009$. Note that *mil*-units are quoted throughout as the standard because all of the fabrication processes were based on their use, but the equivalent value in millimeters is also given. Some useful conversion values are $100 \text{ mils} = 2.54$ mm and the free space wavelength
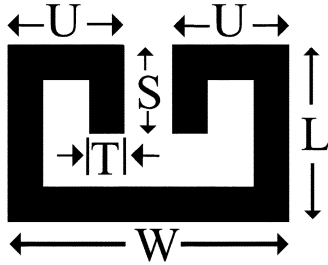
Fig. 1.   Dimensions of each CLL element.

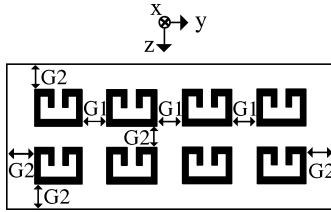Fig. 2.   Two CLL-deep unit cell geometry.

at 10 GHz is $\lambda_0 = 30.0$ mm $= 1\,181$ mils and in a medium with $\varepsilon_r = 2.2$ is $\lambda_m = \lambda_0/\sqrt{2.2} = 20.23$ mm $= 796.30$ mils.

The CLL element and the basic two-element CLL unit cell that were used for our AMC designs are shown, respectively, in Figs. 1 and 2. Like the SRR element, the CLL element is resonant, the resonant frequency being determined mainly by the loop inductance and the capacitance of the strips. The CLL element is much simpler than the two concentric split rings that form the SRR element.

Referring to Fig. 1, all the line widths of the CLL elements were $T = 18$ mils $= 0.457$ mm. The total z-length of each CLL was $L = 100$ mils $= 2.54$ mm. The total y-length of each CLL was $W = 160$ mils $= 4.064$ mm. The z-depth of the capacitive strips of each CLL was $S = 49$ mils $= 1.245$ mm. The y-lengths of each segment of the split side of each CLL was $U = 65$ mils $= 1.651$ mm. Thus, the capacitive gap size was 30 mils $= 0.762$ mm for each CLL. The x-length of each CLL was assumed to be infinitely thin and was treated in HFSS by applying perfect electric conductor (PEC) boundary conditions over each CLL surface, i.e., $\vec{E}_{\tan} = 0$.

Referring now to Fig. 2, an incident plane wave is assumed to propagate toward the unit cell in the $+z$ direction with its magnetic field oriented along the $-x$ axis and its electric field oriented along the $+y$ axis. The basic two-element CLL unit cell assumes that both CLL elements are aligned in the same direction with the gaps facing the incident wave direction. The complete unit cell consists of 8 CLL elements in a 4×2 (relative to the yz axes) array. All of the gaps along the y axis between the CLLs were $G1 = 40$ mils $= 1.016$ mm. The z and y distances between the edge of the CLLs and the unit cell boundaries were $G2 = 20$ mils $= 0.508$ mm. The substrate corresponded to the 31 mil $= 0.787$ mm thick, 1 oz., Rogers 5880 Duroid material used in the fabrication and experiments. It had a relative permittivity and permeabililty, respectively, $\varepsilon_r = 2.2$ and $\mu_r = 1.0$. The plane of the CLLs in the unit cell was centered in the dielectric, 15.5 mils $= 0.394$ mm from either x-boundary. Thus, the total xyz size of the

metamaterial unit cell was 31 mils $\times$ 800 mils $\times$ 260 mils $= 0.787$ mm $\times$ 20.32 mm $\times$ 6.604 mm.

The HFSS simulation space was a rectangular PEC-PMC waveguide whose total xyz size was 31 mils $\times$ 800 mils $\times$ 360 mils $= 0.787$ mm $\times$ 20.32 mm $\times$ 9.144 mm. The metamaterial unit cell was centered in this waveguide. The waveguide walls orthogonal to the y axis were PEC walls; the waveguide walls orthogonal to the x axis were PMC walls. The waveguide walls orthogonal to the z axis were the exciting ports, 50 mils $= 1.270$ mm from the faces of the metamaterial slab. The region inside of the waveguide and outside of the metamaterial slab was assumed to be vacuum, $\varepsilon_r = 1.0, \mu_r = 1.0$. With this configuration, the metamaterial slab acts as a periodic structure of the CLL elements that is infinite in extent in the x and y directions and the excitation acts as a transverse electromagnetic (TEM) plane wave that is incident normal to the metamaterial slab. The HFSS predicted values of S_{11} and S_{21} were de-embedded to the faces of the metamaterial slab.

The initial dimensions of the CLL element and the corresponding unit cell were based on the dimensions successfully used in [12]; they were finalized using the HFSS software tools to achieve the desired in-phase reflection conditions $S_{11} = +1$ at the design frequency 10 GHz. The final design simulations were run for a 20 GHz λ-refinement frequency. The wavelength of the λ-refinement frequency is used to define the size of the tetrahedra in the initial finite element mesh. Successive solution iterations are made relative to this initial mesh. The larger the λ-refinement frequency relative to the frequencies of interest, the higher the mesh resolution will be at those frequencies. Thus, a higher λ-refinement frequency forces HFSS to use more tetrahedra to define the problem. Design simulations of the unit cell were completed with a total number of 11 279 tetrahedra. The S-parameter values were computed with a fast sweep run between 8 and 12 GHz for 401 points. The magnitudes and phases of the HFSS predicted S_{11} and S_{22} results for the two CLL-deep unit cell are shown in Fig. 3. The magnitude values of S_{11} and S_{21} at 10 GHz were -0.003 dB and -31.20 dB, respectively. The phase value of S_{11} goes through zero at 9.92 GHz, hence, the two CLL-deep unit cell behaves like an AMC slab at this frequency. The magnitude values of S_{11} and S_{21} at 9.92 GHz were -0.001 dB and -34.72 dB, respectively. The $\pm 45°$ bandwidth was 1.0 GHz. It is also interesting to note that the magnitude and the phase values of S_{22} at 9.92 GHz were -0.0004 dB and $174°$, respectively. In fact, the S_{22} values exhibit a PEC behavior for the entire X band set of frequencies. Thus, while the CLL-based metamaterial slab looks like an AMC when the incident wave is toward the CLL gaps, it looks like a PEC when the incident wave arrives from the opposite direction toward the solid portion of the CLLs, even though there is no PEC ground plane present.

The same structure was expanded to a four CLL-deep unit cell to test whether more elements would effect the basic AMC properties of the metamaterial slab. As shown in Fig. 4, the four CLL-deep unit cell was constructed simply by putting two, two CLL-deep unit cells together. Note that the distance between the second and third column of CLLs is $2G_2 = 40$ mils $= 1.016$ mm. The behavior of three other alternate configurations of pairs of the two CLL-deep unit cell slab were also studied. One row of
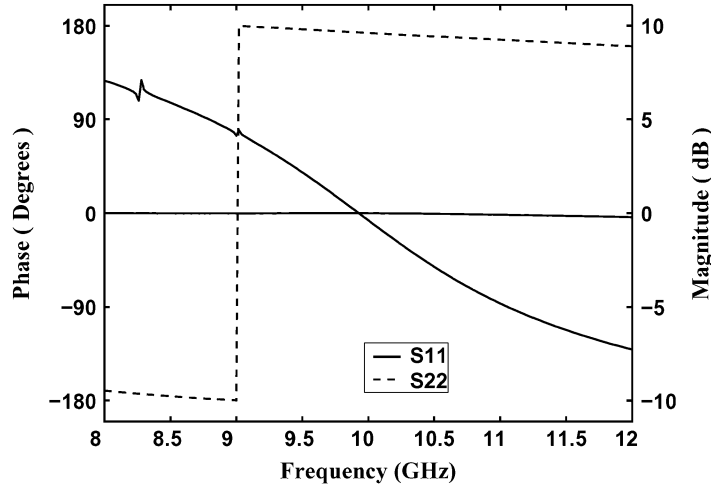
Fig. 3. Magnitudes and phases of the HFSS predicted S_{11} and S_{22} values for the two CLL-deep unit cell across the frequency band of interest, 8–12 GHz. The magnitude values show nearly complete reflection. The S_{11} phase results show an in-phase reflection; the S_{22} phase results show an out-of-phase reflection. The zero crossing of the phase values of S_{11} occurs at 9.92 GHz.
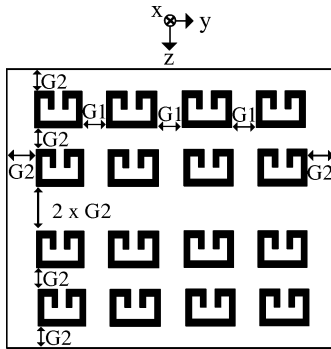

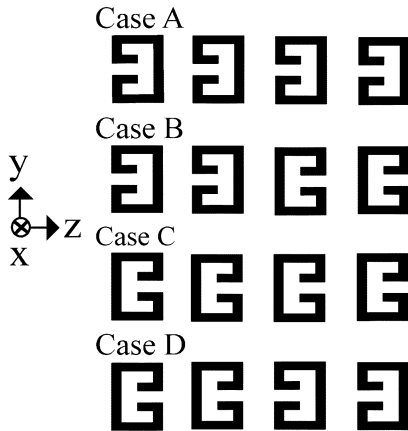Fig. 4. Four CLL-deep unit cell geometry.

Fig. 5. Summary of the four CLL-deep unit cell structures that were investigated.

each structure that was studied is shown in Fig. 5 and is labeled by Case A-D. The simulations were run for a 20 GHz λ-refinement frequency, and they were completed with approximately 13 000 total tetrahedra. The magnitudes and phases of the HFSS predicted S_{11} values for Cases A-D are given in Fig. 6. The magnitude of S_{11}, as was expected, was essentially zero 0 dB (between 0.0 and -0.01 dB from 9 to 11 GHz) for each case

across the frequency band. Cases A and B both show an AMC behavior near 10 GHz. The phase values of S_{11} for both configurations go through zero at 9.73 GHz. The $\pm 45°$ bandwidths for Cases A and B were, respectively, 940 and 930 MHz. The Case B S_{11} phase values also have a more oscillatory behavior across the frequency range than their Case A counterparts. We believe that this result is caused by the coupling between the second and third columns of the CLL elements. These structures are placed back to back in Case B, and, thus, they show greater capacitive characteristics. Moreover, there will be some cancellation of the local magnetic field behaviors between columns one and two and columns three and four because they are oriented oppositely. This also cancels some of the bianisotropy associated with a single CLL. Cases C and D both failed to show any AMC behavior at the simulation frequency range. In fact, they acted like artificial electric conductor (AEC) slabs near 10 GHz. We believe that this is a result of the capacitance gaps not being exposed directly to the incident field; and, hence, the effective capacitance is much less, raising the resonant frequency outside of the range of interest.

The final HFSS simulation was an exact model of the measured CLL structure and the actual experimental configuration. The two CLL-deep metamaterial block was formed by stacking 31 unit cells together along the x axis and, hence, contained 248 CLL elements. The metamaterial block, thus, had the xyz dimensions: 961 mils $\times$ 800 mils $\times$ 260 mils $=$ 24.41 mm $\times$ 20.32 mm $\times$ 6.604 mm. This finite sized metamaterial (MTM) block was placed between two X band waveguides. The corresponding HFSS simulation space is shown in block diagram form in Fig. 7. The experimental configuration simply connected the network analyzer to the ports, i.e., to the sources at the outer ends of the waveguides. The dimensions of the selected waveguide was 900 mils $\times$ 400 mils $=$ 22.86 mm $\times$ 10.16 mm. The waveguide length from the ports at the outside ends of the waveguides to the faces of the metamaterial block was 100 mils $=$ 2.54 mm. Because the metamaterial block is an open structure, energy can be radiated out the sides of the block. A vacuum box was created in the simulation region that was
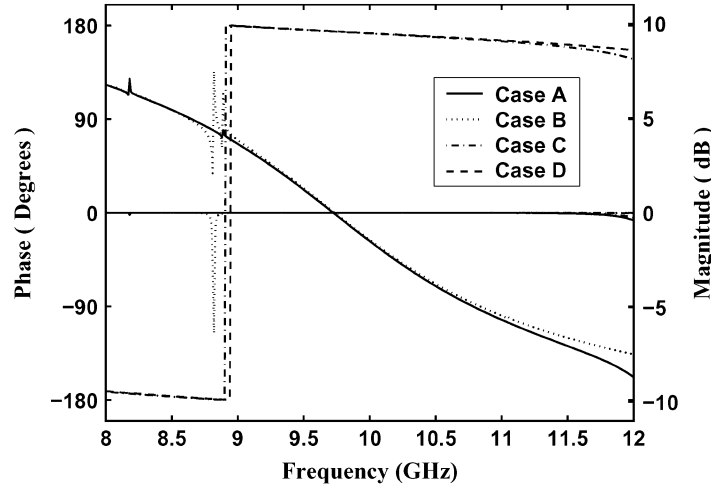
Fig. 6. Magnitudes and phases of the HFSS predicted S_{11} values for the four CLL-deep Cases A-D are shown. The phases of Cases A and B have zero crossings at 9.73 GHz; hence, they act as artificial magnetic conductors there. The phases of Cases C and D indicate that they act primarily as artificial electric conductors in this frequency region.
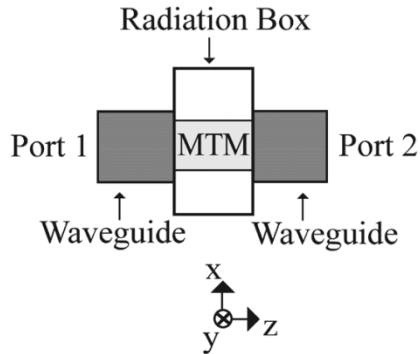

Fig. 7. Block diagram of the HFSS simulation of the finite two CLL-deep metamaterial (MTM) block excited by two X band waveguides.

Fig. 8. CAD diagram of the waveguide excitation of the finite two CLL-deep metamaterial block.

centered on the metamaterial block and radiation boundary conditions were assumed on all exposed faces of the block. The box had the xyz dimensions: $1\,061$ mils $\times$ 900 mils $\times$ 360 mils $=$ $26.949\,\text{mm} \times 22.86\,\text{mm} \times 9.144\,\text{mm}$, i.e., it was 50 mils $= 1.27$ mm larger than the metamaterial block in all directions. The HFSS simulation model thus, included possible radiation leakage out through the open structure in all directions. The placement of the CLL structure relative to the waveguide is shown in Fig. 8. A (PEC) symmetry plane was used along the (xz) plane to increase the computational efficiency.

The HFSS simulation of the finite block model required 59 163 tetrahedra. The maximum magnitude of the complex difference between all of the S-parameters obtained with the current mesh refinement and the corresponding ones from the previous mesh, ΔS, was 0.02 for a 20 GHz λ-refinement frequency. The magnitudes and phases of the S_{11} and S_{21} values were again computed with a fast sweep calculated between 8 and 12 GHz for 401 points. The HFSS predicted magnitudes and phases of S_{11} and S_{21} were de-embedded to the outside faces of the substrate along the z axis. The magnitudes and phases of the HFSS predicted S_{11} values for the finite two CLL-deep metamaterial block are shown in Fig. 9. The magnitude value of S_{11} at 10 GHz was -0.16 dB. The phase value of S_{11} goes through zero at 9.86 GHz, hence, the finite two CLL-deep AMC block behaves like
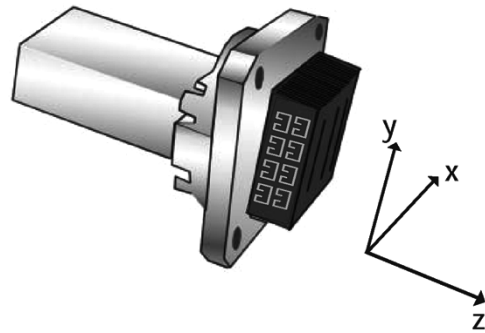
an AMC at this frequency. The magnitude value of S_{11} at 9.86 GHz was -0.1 dB. The $\pm 45°$ bandwidth was 800 MHz. It is also interesting to note that the magnitude and the phase values of S_{22} at 9.86 GHz were -1.0 dB and $167°$, respectively. Again, the slab acts like an AMC from one direction and as an AEC from the other. The magnitude and phase values of the computed S_{11} values for the finite block were -0.099 dB and -0.06 GHz different, respectively, from the infinite slab results. The tolerable differences between the block and slab simulation cases were caused by the angle of incidence of the incident wave, i.e., the finite simulation model of the finite block was excited using the dominant TE_{10} mode in a X band waveguide, while the infinite slab was excited with a TEM plane wave.

III. Fabrication

There are four main stages in the fabrication process of the CLL structures using the Roger's 5880 Duroid™. These stages are: 1) spinning and coating the board with photoresist; 2) exposing the board to UV light; 3) developing; and 4) etching. All of the processing was accomplished in the MicroElectronics Laboratory located in the Department of Electrical and Computer Engineering at the University of Arizona. Originally, we attempted to develop an air-brush technique to coat the boards. This approach was found to significantly save on the amounts of
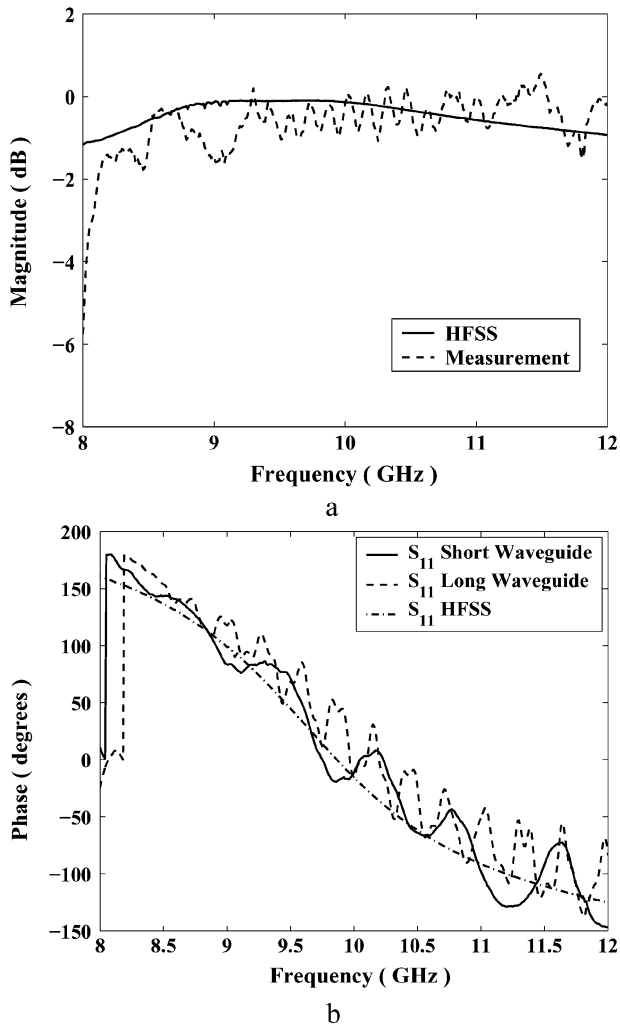
Fig. 9. HFSS predicted and the measured S_{11} values for the finite two CLL-deep metamaterial block. As predicted, nearly complete reflection occurs near the target frequency. The phase of the measured S_{11} values crosses zero at 9.75 GHz, 1.02% different from the HFSS predicted value, 9.86 GHz. (a) Magnitudes and (b) phases.

the photoresist that were being used in the processing. However, the air-brush approach was found to be unsatisfactory because it was difficult to achieve a thin, uniform coating. Because of the board sizes, a standard spinner was used for the final fabrication process. It gave a coat with a thickness between 1.0 and 1.5 microns versus the 4 to 5 micron thickness that was achieved with the airbrush. A three-inch by three-inch board size was selected and it yielded 14 two CLL-deep unit cell structures. After spinning, the boards were placed in a 100°C furnace for one minute to dry them. The printed mask of the design was generated and placed over the board. The boards were then exposed for 1.5 min with UV light. The boards were then placed in a developer. Developing time was under one minute. Once the photoresist was removed, the boards were rinsed with deionized water and dried with nitrogen. Finally, the boards were placed in a Ferric Chloride etching solution. This process took between 10 and 15 min to complete, exercising care to not over-etch the boards. The boards were rinsed with acetone to remove any remaining photoresist from the board. The boards were finally rinsed with deionized water and dried with nitrogen.

The boards were inspected under a microscope and the best ones were selected. Alignment holes had been inserted at the y ends of the two CLL-deep unit cells when the mask was designed. The boards were cut and drilled professionally in the University of Arizona machine shop. A large number of the two CLL-deep unit cells were fabricated. Threading polyethylene rods through the alignment holes, two 31 layer metamaterial stacks were formed. The four CLL-deep structures were obtained by stacking these two, two CLL-deep metamaterial blocks together in the Case *A-D* configurations.

IV. EXPERIMENTAL RESULTS

The fabricated metamaterial blocks were measured using an HP8720C network analyzer. A 3.5 mm HP calibration kit was used to calibrate the network analyzer. A full 2-port calibration was performed using the short-open-load-thru (SOLT) method. The calibration was done between 8 and 12 GHz for 401 points. The S_{11} value of a HP 902D broadband load was measured to confirm the accuracy of the calibration method. Two *X* band waveguides were used to excite the metamaterial blocks. The S_{11} and S_{21} values were measured with the network analyzer.

To obtain an accurate measurement of the phases, it was decided to use a reference case consisting of a copper plate located where the front face of the metamaterial block would be when it was measured. Note that the metamaterial block simply rests against the face of the waveguide aperture as shown in Fig. 8. The copper plate was positioned in a similar manner. The S_{11} and S_{21} values were obtained for both the copper plate and the metamaterial block. The relative phases between the reference case and the metamaterial block cases were obtained and unwrapped so that the phase angles occurred primarily in the $[-\pi, \pi]$ interval over the measured frequency band. The metamaterial block was measured with both a short, $4\,000\,\text{mils} = 101.6\,\text{mm}$ long, and a long $13\,000\,\text{mils} = 330.2\,\text{mm}$ waveguide section to minimize the effects of their lengths on the phase measurements.

The relative magnitudes and phases of the measured S_{11} values for the two CLL-deep metamaterial block are compared to the corresponding HFSS predicted values in Fig. 9. Good agreement between the measured and predicted S_{11} magnitude values was obtained. The measured S_{11} magnitude and phase values at 10 GHz were -0.17 dB and $-10.83°$. These results were close to the HFSS predicted values of -0.16 dB and $-15.46°$. The measured phase of S_{11} crosses zero at 9.75 GHz, 1.02% different from the predicted value. The measured $\pm 45°$ bandwidth was 780 MHz. The measured S_{11} and S_{21} magnitude values at 9.75 GHz were -0.25 dB and -48 dB, respectively. These values reflect the fact that the finite block is an open structure (in both the experiments and the HFSS simulations) and some power is lost by scattering out of the faces of the block parallel to the waveguide direction.

The magnitudes and phase of S_{11} values for Cases *A-D* were also obtained. These results are shown in Fig. 10. Some of the S_{11} magnitude values for the two CLL-deep metamaterial block shown in Fig. 9(a) and for the four CLL-deep metamaterial block Cases *A* and *B* shown in Fig. 10(a) slightly exceeded the 0
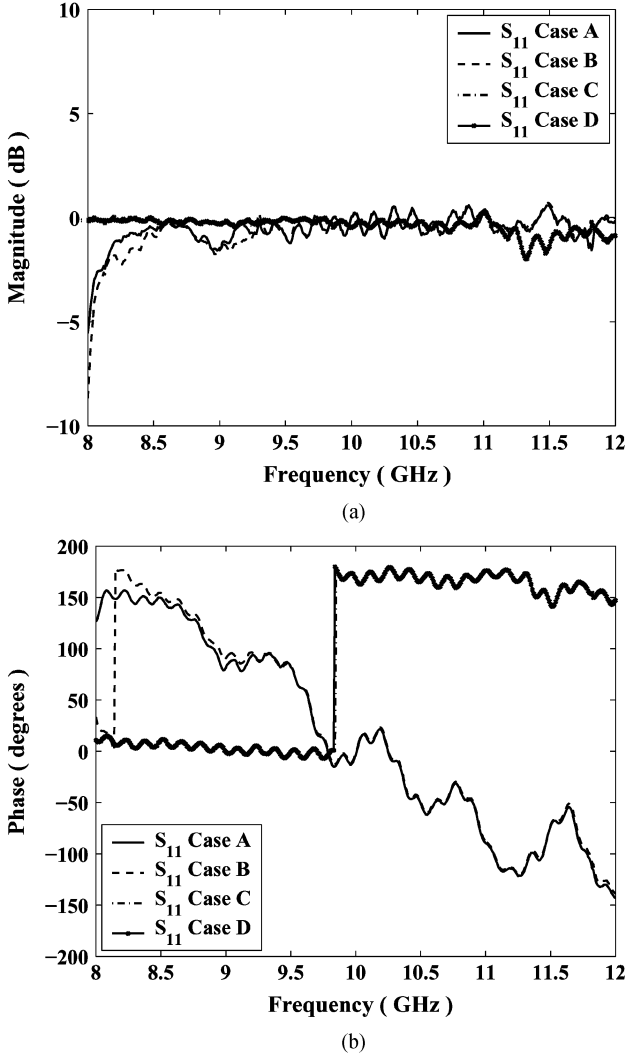
Fig. 10.   Measured S_{11} values for the finite versions of Cases A-D are shown. As predicted, nearly complete reflection occurs near the target frequency. The phases of the measured S_{11} values for the finite versions of Cases A-D show, as predicted, that Cases A and B have zero crossings while Cases C and D do not. Cases A and B act as artificial magnetic conductors; Cases C and D act as artificial electric conductors. The AMC zero crossing was measured at 9.785 GHz, 0.57% different from the predicted value. (a) Magnitudes and (b) phases.

dB level. Because the values are relative to the copper plate measurements, these anomalies are due simply to the noise in the measurements. The measured S_{11} magnitude and phase values at 10 GHz for Case A were 0.05 dB and $-6.86°$. The predicted results for this case were -0.0002 dB and $-38.0°$. The measured S_{11} magnitude and phase values at 10 GHz for Case B were 0.01 dB and $-1.67°$. The predicted results for this case were -0.002 dB and $-14.4°$. The zero crossings for Cases A and B were measured at 9.785 GHz, 0.57% different from the predicted value. The measured S_{11} magnitude values for cases A and B were -0.56 dB and -0.62 dB, respectively. The measured $\pm45°$ bandwidth for both of these cases was 830 MHz. As predicted, Cases C and D failed to show any AMC properties; rather they showed the anticipated AEC properties.

We note that the two CLL-deep metamaterial blocks had better agreement in general with the HFSS predictions in comparison to the four CLL-deep metamaterial cases. The dif-

ferences between them are due to fabrication issues. The four CLL-deep metamaterial cases were obtained simply by putting two of the two CLL-deep metamaterial blocks back-to-back with the specified element orientations shown in Fig. 5. As a result, there were nontrivial air gaps between the two blocks and their impact on the results are noticeable.

We also note that we measured the two CLL-deep metamaterial block with it being oriented orthogonal to the desired direction, i.e., with the plane of the CLL elements parallel to the magnetic field direction. The CLL elements are strongly anisotropic. In particular, if the magnetic field were parallel to the plane of the CLL elements, the strong inductance and, hence, the resonant effect should disappear and the highly reflective block should become highly transmissive. The measured magnitudes of S_{11} and S_{21} for this orthogonal orientation at 10 GHz were, respectively, -21.46 dB and -0.8 dB. These results confirm that the metamaterial structure is indeed anisotropic and that the orientation of the metamaterial block relative to the exciting magnetic field is critical to the realization of the predicted AMC behavior.

V. EFFECTIVE MATERIAL PROPERTIES

While the reflection and transmission properties of the CLL-based AMC slab were obtained directly from numerical simulations, the effective permittivity and permeability of the slab must be extracted from this scattering data. We have found using the extraction method proposed in [12] that an equivalent material model of the CLL-based AMC consists of a two time derivative material (2TDLM) model for the permeability and a Drude model for the permittivity. The resonance, f_{res}, of the real part of the 2TDLM model and the zero crossing, f_p, of the real part of the Drude model occur at the frequency, f_{crit}, for which the in-phase reflection occurs, i.e., for $f_{\text{res}} = f_p = f_{\text{crit}}$. This concurrence of the critical frequencies of both models produces a metamaterial slab with a high-Z/low-n state at f_{crit}. To investigate these results further, we have used the HFSS S-parameter results and the 2TDLM and Drude models to develop a model-based parameter estimation of the permittivity and permeability values.

We note that the SRRs have been shown to have a bianisotropic nature, primarily due to the presence and coupling of the two split rings [18]. We have not attempted to account for any such magnetoelectric contributions in our models. The HFSS simulation results include all such effects. Because the extracted material properties reproduce the scattering parameter results quantitatively, this appears to be a reasonable approach.

The 2TDLM model has been used for several metamaterial investigations, e.g., [12], [19]. It was used to design an artificial molecule realization of a magnetic wall in [20]. The 2TDLM model is the natural description of many of the SRR inclusions incorporated to achieve the artificial magnetic properties in DNG metamaterials. The 2TDLM medium is a causal medium that satisfies a generalized Kramers–Krönig relation and is specified by its susceptibility in the frequency domain through the relation [19]

$$\chi_{2\text{TDLM}}(\omega) = \frac{-\omega^2 \chi_\gamma + j\omega_p \chi_\beta \omega + \omega_p^2 \chi_\alpha}{-\omega^2 + j\Gamma_m \omega + \omega_{\text{res}}^2}. \qquad (6)$$

In contrast, the Drude model is associated with lossy cold electron plasmas, which can be realized artificially with a "bed of nails" medium (e.g., [10], [11]) and a CLS medium [19]. The susceptibility of a lossy Drude medium is given by the expression

$$\chi_{\text{Drude}}(\omega) = \frac{\omega_p^2}{-\omega^2 + j\Gamma_e\omega}. \tag{7}$$

We introduce a model medium that incorporates these properties by specifying the magnetic permeability and the electric permittivity, respectively, as

$$\mu(\omega) = L_\mu\mu_0[1 + \chi_{\text{2TDLM}}(\omega)]$$
$$\varepsilon(\omega) = L_\varepsilon\varepsilon_0[1 + \chi_{\text{Drude}}(\omega)]. \tag{8}$$

The additional positive constants, L_μ and L_ε, are introduced to allow for relative constant levels of both the permeability and permittivity in the fitting process. With this composite model the magnetic permeability is resonant at $f_{\text{res}} = \omega_{\text{res}}/2\pi$, and the permittivity has a zero crossing at the plasma frequency $f_p = \omega_p/2\pi$. Consequently, the 2TDLM model produces a large negative (positive) permeability just above (below) the resonant frequency; the Drude model produces a negative (positive) permittivity just below (above) the plasma frequency. If $f_{\text{res}} = f_p$, the critical frequency represents the boundary between the main ENG (epsilon negative) and the MNG (mu negative) frequency regions. Moreover, at $f_{\text{crit}} = f_{\text{res}} = f_p$, the wave impedance $\eta = \eta_0\sqrt{L_\mu/L_\varepsilon}\sqrt{1 + \chi_{\text{2TDLM}}}/\sqrt{1 + \chi_{\text{Drude}}} \to \infty$ and the index of refraction $n = \sqrt{L_\mu L_\varepsilon}\sqrt{1 + \chi_{\text{2TDLM}}}\sqrt{1 + \chi_{\text{Drude}}} \to 0$.

The 2TDLM and Drude model-based parameter-estimation of the S-parameters was accomplished using the MATLAB Optimization Toolbox. The model parameters were fit to the corresponding HFSS predicted S_{11} and S_{21} results for a unit cell of the CLL-based metamaterial AMC excited in the PEC-PMC waveguide simulator using a nonlinear least-squares optimization method, where we used only the S_{11} values to fit the model parameters. The optimization scenarios using both S-parameter values produced less matched results due to the very small S_{21} values. With the optimized match of the S_{11} results, the S_{21} effective medium results also showed reasonable agreement with the original HFSS predicted values. These optimized 2TDLM parameters were $\chi_\alpha = 0.1, \chi_\beta = 1.0 \times 10^{-4}, \chi_\gamma = -0.973\,23, \Gamma_m = 1.0 \times 10^{-5}\omega_{\text{res}}, L_\mu = 0.639\,43$ and $f_{\text{res}} = 10.0019$ GHz; and the corresponding Drude parameters were $\omega_p = \omega_{\text{res}}, L_\varepsilon = 10$, and $\Gamma_e = 1.0 \times 10^{-5}\omega_p$. This means $f_{\text{res}} = f_p = f_{\text{crit}}$, as expected. The resulting real and imaginary parts of the permittivity and permeability are shown, respectively, in Fig. 11. The permittivity losses are essentially zero in this region; the permeability losses are restricted to a very narrow region near the resonance frequency. The permittivity and permeability have opposite signs on either side of the resonance frequency yielding evanescent wave properties, hence, high reflectivity. The magnitude of the permeability (permittivity) is large (small) in this frequency interval. Thus, the CLL-based unit cell for a normally incident plane wave in the indicated frequency range acts as a high-Z/low-n material at f_{crit}, yielding $S_{11} = +1$ near the frequency of interest. This effective magneto-dielectric medium model for the CLL-based
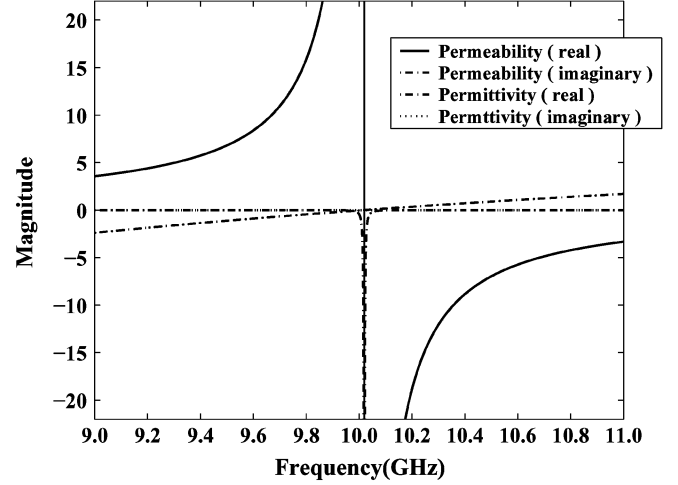

Fig. 11. Real and imaginary parts of the model-based estimation of the permeability and permittivity that optimally recover the CLL-based AMC unit cell S-parameters.

metamaterial slab was also verified by considering the parameter extraction method discussed in [14]. Reasonable agreement with all of the fitted model results was obtained. Finally, similar conclusions were reached for the two-CLL and four-CLL deep metamaterial slabs.

VI. DIPOLE ANTENNA AND CLL-BASED ARTIFICIAL MAGNETIC CONDUCTOR BLOCK INTERACTIONS

The dipole antenna, CLL-based metamaterial slab interactions were simulated with HFSS. A 10 GHz dipole antenna was positioned symmetrically at the origin of the coordinate system and oriented along the z axis. Three different dipole lengths were studied: a) $0.08\lambda_0$ (94.488 mils = 2.40 mm); b) $0.325\lambda_0$ (383.85 mils = 9.750 mm); and c) $0.5\lambda_0$ (590.55 mils = 15.0 mm), recalling that $\lambda_0 = 30.0$ mm at 10 GHz. Each dipole antenna was modeled using two identical cylinders with a radius of $0.0033\lambda_0$ (3.937 mils = 0.10 mm). The cylinders were defined as perfect electric conductors, and the total distance between the two cylinders was optimized for each dipole antenna to obtain the analytical radiation results that were given in [21]. The optimized gap spaces for $0.08\lambda_0, 0.325\lambda_0$, and $0.5\lambda_0$ length dipole antennas were 0.0374 mils = 0.000 95 mm, 19.68 mils = 0.500 mm, and 35.43 mils = 0.900 mm, respectively. Another vacuum filled cylinder was also used to fill the gap between the two dipole arms. The current distribution of the dipole was excited across this vacuum cylinder using the HFSS current source, and it was assumed to be constant with an amplitude of 1 A.

The unit cell of the two-element CLL-based metamaterial block was now taken to be 10 CLL elements in a 5×2 array, with the five CLLs being taken along the z direction. The y and z distances between the edges of the CLLs and the unit cell boundaries were still maintained at $G2 = 20$ mils = 0.508 mm; the distances between each CLL element were still maintained at $G1 = 40$ mils = 1.016 mm. The CLL elements were centered in the dielectric 15.5 mils = 0.394 mm from either x-boundary. Thus, its total xyz size was 31 mils × 260 mils × 1 000 mils = 0.787 mm × 6.604 mm × 25.4 mm.

TABLE I
SUMMARY OF THE DIPOLE ANTENNA, CLL-BASED ARTIFICIAL MAGNETIC CONDUCTOR SLAB RESULTS OPTIMIZED FOR THE COMBINATION OF THE DIPOLE
LENGTH AND DISTANCE OF THE DIPOLE FROM THE SLAB

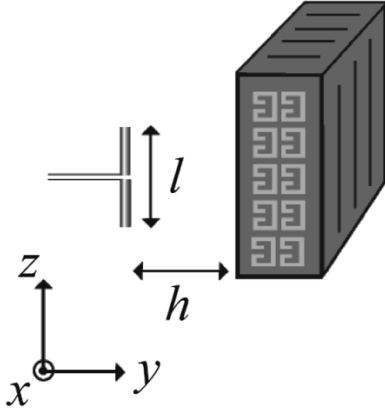| Dipole length (in λ_0)	Distance	Resonant Frequency (GHz)	E_{max} (V)	E_{max} / $E_{free-space}$	Front-to-Back Ratio (dB)
0.08	λ_0 / 15	9.893	47.75	6.26	33.89
0.325	λ_0 / 25	9.987	75.49	2.29	44.31
0.5	λ_0 / 16	9.403	63.45	1.22	15.31

Fig. 12. CAD diagram of the dipole antenna and the finite two CLL-deep metamaterial block.

The two CLL-deep metamaterial block was then formed by stacking 7 unit cells together along the x axis and, hence, contained 70 CLL elements. The two-element CLL-based metamaterial block, thus, had the xyz dimensions: $217\,\mathrm{mils} \times 260\,\mathrm{mils} \times 1\,000\,\mathrm{mils} = 5.512\,\mathrm{mm} \times 6.604\,\mathrm{mm} \times 25.4\,\mathrm{mm} = 0.18\lambda_0 \times 0.22\lambda_0 \times 0.85\lambda_0$. The face of the two-element CLL metamaterial slab was oriented parallel to the zx plane with the capacitor gaps of the CLLs facing the dipole. The center of the slab, hence, one set of CLLs was placed in the yz plane. The centers of the gaps of the middle CLLs in this plane were centered on the y axis. Thus, the dipole and all the CLLs are symmetrically located with respect to each other. The field radiated by the dipole propagates along the $+y$ direction toward the center of the CLL metamaterial slab and the main beam of the reflected field propagates along the $-y$ direction.

The dipole and this finite-sized CLL-based metamaterial block were positioned symmetrically about the xy plane, and the front face of the finite-sized metamaterial block was placed a distance h away from the dipole (from the origin) along the positive y axis as shown in Fig. 12. A free-space radiation box was created that was centered at the origin. It had the xyz dimensions: $1\,732\,\mathrm{mils} \times 1\,732\,\mathrm{mils} \times 1\,732\,\mathrm{mils} = 43.993\,\mathrm{mm} \times 43.993\,\mathrm{mm} \times 43.993\,\mathrm{mm}$. The dimensions of the radiation box satisfied the ANSOFT recommended $0.25\lambda_0$ ($295.28\,\mathrm{mils} = 7.50\,\mathrm{mm}$) distance from the metamaterial block to the free-space radiation box in all directions. More specifically, the distance between the free-space radiation box and the metamaterial block was $726.5\,\mathrm{mils} = 18.453\,\mathrm{mm}$ in the $\pm x$ directions and $366\,\mathrm{mils} = 9.296\,\mathrm{mm}$ in the $\pm z$ directions. With, for instance, the largest h value considered, $h = 0.25\lambda_0$ ($295.28\,\mathrm{mils} = 7.50\,\mathrm{mm}$), the distance between the front of the metamaterial block and the free-space radiation box along the

$-y$ axis was $866 + 295 = 1\,161\,\mathrm{mils} = 29.489\,\mathrm{mm}$ and the distance between the back face of the metamaterial block and the free-space radiation box in $+y$ axis was $311\,\mathrm{mils} = 7.899$ mm. A (PEC) symmetry plane was then introduced along the (xy) plane to increase the computational efficiency.

The interaction of the dipole antenna and the metamaterial block was studied by varying h and the length of the dipole ℓ. A total of 15 different cases were studied: three dipole lengths were tested for five different h values. The simulated dipole lengths were: 1) $\ell = 0.08\lambda_0$ ($94.49\,\mathrm{mils} = 2.40\,\mathrm{mm}$), whose equivalent monopole length is just larger than half of the first half CLL; 2) $\ell = 0.325\lambda_0$ ($383.86\,\mathrm{mils} = 9.750\,\mathrm{mm}$), whose equivalent monopole length is just smaller than the height to the middle of the first whole CLL; and 3) $\ell = 0.5\lambda_0$ ($590.55\,\mathrm{mils} = 15.0\,\mathrm{mm}$), whose equivalent monopole length is just larger than the height of the second whole CLL. The simulated distances between the dipole and the block were: (1) $h = \lambda_0/50$ ($23.62\,\mathrm{mils} = 0.60\,\mathrm{mm}$), (2) $h = \lambda_0/25$ ($47.24\,\mathrm{mils} = 1.20\,\mathrm{mm}$), (3) $h = \lambda_0/16$ ($73.81\,\mathrm{mils} = 1.875$ mm), (4) $h = \lambda_0/15$ ($78.74\,\mathrm{mils} = 2.0\,\mathrm{mm}$), and (5) $h = \lambda_0/4$ ($295.28\,\mathrm{mils} = 7.50\,\mathrm{mm}$).

The far field electric field values and the corresponding amplitude patterns were calculated for the dipole alone and with the metamaterial block present. The maximum values of the electric field in the two directions broadside to the metamaterial block were obtained. The maximum electric field value, E_{max}, was found always to be along the y axis in the reflected, $-y$-direction. The electric field value at $180°$ with respect to the maximum electric field direction, $E_{\mathrm{antipodal}}$, was obtained. It was along the y axis in the $+y$ direction, behind the metamaterial block. The front-to-back ratio; i.e., $\mathrm{front-to-back\ ratio} = E_{\mathrm{max}}/E_{\mathrm{antipodal}}$, was then calculated. The free-space calculations allowed us to verify the validity of the HFSS predicted field values by comparisons with known analytical results; the expected values were recovered in each case. They also provided us with values to compare against when the metamaterial block was present.

The maximum front-to-back ratios obtained when the distance h was varied for each of the three dipole length cases are summarized in Table I. For each of these cases, the HFSS simulation specifics were: 1) $\ell = 0.08\lambda$ dipole antenna was positioned $h = \lambda_0/15$ away from the metamaterial block. The HFSS simulation required 101 179 tetrahedra and produced a variation of $\Delta S = 0.05$ for a 20 GHz λ-refinement frequency. 2) $\ell = 0.325\lambda$ dipole antenna was positioned $h = \lambda_0/25$ away from the block. The HFSS simulation required 108 310 tetrahedra and produced a variation in the S-parameters of $\Delta S =$
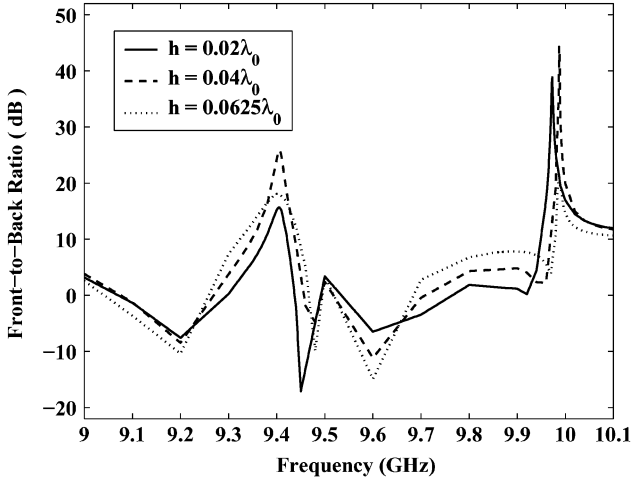
Fig. 13. HFSS simulations demonstrate that by tuning the distance h of the $0.325\lambda_0$ dipole from the two element CLL-based block, the front-to-back ratio can be enhanced significantly.

0.06 for a 20 GHz λ-refinement frequency. 3) $\ell = 0.5\lambda$ dipole antenna that was positioned $h = \lambda_0/16$ away from the block. The HFSS simulation required 104 384 tetrahedra and produced a variation in the S-parameters of $\Delta S = 0.05$ for a 20 GHz λ-refinement frequency. The simulated pattern was computed with a discrete sweep between 9.0 and 10.1 GHz using a 0.001 GHz resolution frequency in each of the cases.

It was found that there was a resonant response of the dipole antenna and the CLL-based metamaterial block tuned by the distance between them. This resonance phenomena is illustrated with the $\ell = 0.325\lambda_0$ dipole results in Fig. 13. The front-to-back ratios are plotted for the various distances between the dipole and the metamaterial block. The resonant behavior is clearly seen. As found from Table I, the obtained resonant frequencies for the $\ell = 0.08\lambda_0$ and $\ell = 0.325\lambda_0$ dipole antennas were close to, but above the operating point of the CLL-based AMC block by itself. The resonant frequency of the $\ell = 0.5\lambda_0$ dipole antenna case was considerably below that operating point. This phase difference behavior was expected from the studies in [15]–[17]. Consider a transmission line representation of the dipole-block system. Since the magnitude of the reflection coefficient at the block near its operating frequency is one, it can be represented in the form $\Gamma_L = \exp(j\psi)$, hence, the equivalent circuit element of the block is the load $Z_L = \eta_0(1 + \Gamma_L)/(1 - \Gamma_L) = j\eta_0 \cot \psi$. Consequently, the input impedance of the air gap and the metamaterial block at the dipole is

$$Z_{\text{in}} = j\eta_0 \tan \left(\frac{\pi}{2} - \psi + k_0 h \right). \tag{9}$$

Recall from the HFSS results that above (below) the operating point, the phase of the reflection coefficient was negative (positive). Thus, the $\ell = 0.08\lambda_0$ and $\ell = 0.325\lambda_0$ cases have $\psi < 0$, which means the input impedance seen by the dipole matches its own impedance, i.e., it is capacitive. Maximum power is then transferred to the in-phase, totally reflecting metamaterial block and no power is available for the back direction. Similarly, because the $\ell = 0.5\lambda_0$ dipole is inductive, the resonance occurs where the phase angle is large positive, making the input impedance inductive. Additionally, because the $\ell = 0.5\lambda_0$
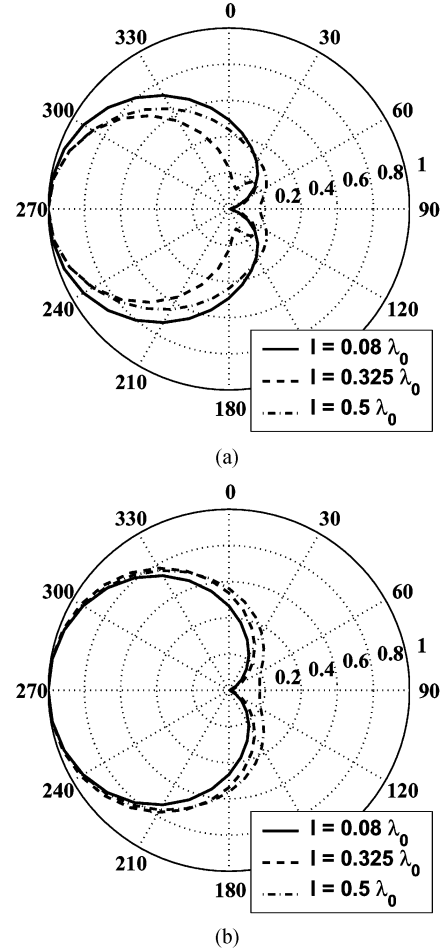

(a)

(b)

Fig. 14. HFSS predicted normalized field patterns generated for the $0.08\lambda_0, 0.325\lambda_0$, and $0.50\lambda_0$ dipole antennas when they are in resonance with the two element CLL-based AMC block system: (a) normalized E plane and (b) normalized H plane patterns.

dipole antenna is nearly as tall as the block itself, significant edge interactions pull the resonant frequency even lower.

We also found that the strength of the resulting enhancements and the radiation pattern was directly connected to the length of the dipole and its interactions with the CLLs. The E plane and H plane electric field patterns of the $\ell = 0.08\lambda_0, \ell = 0.325\lambda_0$, and $\ell = 0.50\lambda_0$ dipole antennas were obtained for the optimized cases and were normalized to their E_{max} values. They are plotted, respectively, in Fig. 14(a) and (b). Comparisons of the normalized E plane and H plane electric field patterns generated by this $0.325\lambda_0$ dipole-block system and by the $0.325\lambda_0$ dipole alone in free space are shown, respectively, in Fig. 15(a) and (b). The corresponding results for the CLL-based metamaterial block replaced by an infinite PMC ground plane, the ground plane coinciding with the block face closest to the dipole antenna, were calculated analytically and are also included in Fig. 15(a) and (b). Fig. 14(a) and (b) show that the antenna field patterns resulted in a deep null in the back direction for the $\ell = 0.08\lambda_0$ and $\ell = 0.325\lambda_0$ cases. This deep null leads to the very large realized front-to-back ratios. The block removed the usual antipodal backlobe found with such finite small ground plane-like structures. The small lobes in the E plane pattern in the back hemisphere of the $\ell = 0.325\lambda_0$ case are associated with the edges of the block. In particular, recall that
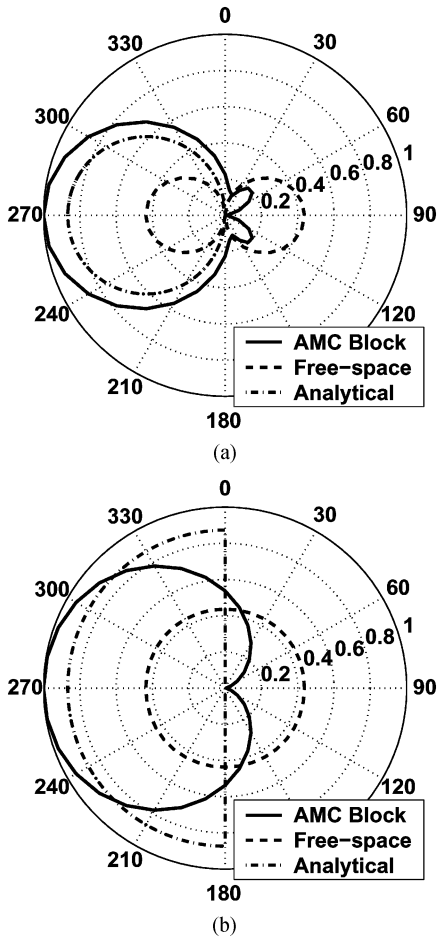
Fig. 15.   HFSS predicted normalized field patterns generated by the $0.325\lambda_0$ dipole antenna when it is in free space, when it is over an infinite PMC ground plane, and when it is in resonance with the two element CLL-based AMC block system: (a) normalized E plane and (b) normalized H plane patterns.

the E plane (H plane) front and back edges of the block are only $0.85\lambda_0(0.18\lambda_0)$ long. The depth of the block is $0.22\lambda_0$; the dipole is $0.04\lambda_0$ from the block for the resonant interaction. Thus, the angle subtended by the top (bottom) edge of the back of the block and the ends of the dipole is $45.3°$. The peak of the small sidelobe in the back direction occurs at $45.0°$ in reasonable agreement with expectations from the finite size of the block.

The field values showed a slightly better value, 2.29, than the expected 2-fold enhancement of the reflected field exhibited by the ideal infinite PMC ground plane case. Because the $\ell = 0.325\lambda_0$ dipole interacted more uniformly with all of the CLL elements in the block, it had the best front-to-back ratio, $44.31\text{ dB} = 164.25$. The smaller $\ell = 0.08\lambda_0$ dipole antenna results were very similar. However, because the dipole interacts directly with fewer elements, the front-to-back ratio was only $33.89\text{ dB} = 49.47$. On the other hand, once the block is in resonance with this smaller dipole, its patterns have no sidelobes in the back direction and the block significantly enhances the reflected field maximum, 6.26, over its free space value. The front-to-back ratio decreased substantially for the $\ell = 0.5\lambda_0$ dipole antenna for the fixed metamaterial block height. The resonance effects of the larger dipole are weakened by the edge interactions. The patterns show a coalescence of the two small

back lobes seen in the $\ell = 0.325\lambda_0$ case into one larger one with its maximum being in the back direction. The reflected field is also decreased resulting in only a slightly better value, 1.22, than the free space value. Nonetheless, it is anticipated that a larger, specifically designed block would provide a performance enhancement similar to the $\ell = 0.325\lambda_0$ case.

We emphasize that the distance of the dipole from the block to achieve the resonant interaction in all of the cases was significantly smaller than a wavelength. Moreover, despite the sub-wavelength size of the block, the front-to-back ratios in the highly resonant cases are much better than those associated with many standard antennas, particularly those situated near a ground plane or other conducting structures. However, if further enhancements of the broadside E plane or H plane directivities were desired, the size of the block would have to be increased to allow for some sort of texturing of its surface or the insertion of additional structures. In this manner one could achieve soft or hard surface effects or electromagnetic bandgap effects that would allow one to redirect some of the side and back-directed field energy in the E or H plane toward the broadside direction. The dipole-block interactions would have to retuned for any such modified configuration.

Finally, we show the HFSS predicted near-field electric field distributions in the yz- and xy-planes for the $\ell = 0.325\lambda_0$ case at its resonance $f = 9.987$ GHz in Fig. 16(a) and (b), respectively. The front-to-back ratio of the magnitude of the electric field along the y axis at a point $-1.2\text{ mm} = -47.24$ mils away from the dipole (2.4 mm in front of the CLL-based metamaterial block) and at a point $+9.004\text{ mm} = 354.49$ mils from the dipole (1.2 mm behind the block) is 50.46, i.e., the field behind the AMC block in the backward direction is 34 dB smaller than it is away from dipole toward the forward direction. Thus, the CLL-based metamaterial block provides very good isolation between its front and back sides even in the near-field.

VII. CONCLUSION

A CLL-based metamaterial block was designed to act as an AMC at 10 GHz. Both finite and infinite versions of the block were considered. The finite-sized block was fabricated and tested experimentally in a free-space configuration. Good agreement between the simulation and experimental results was demonstrated. The two CLL-deep metamaterial AMC slab produced in-phase reflections near the predicted frequency when the gaps of the CLL elements were facing the source. Although there was no ground plane backing the slab, it nonetheless acted as an AEC and produced out-of-phase reflections when the waves were incident from the opposite direction. Four CLL-deep metamaterial AMC blocks were also considered. It was shown that the orientation between each of the CLL elements and the incident field was critical to obtaining the desired AMC performance. The $\pm 45°$ bandwidth was approximately 10% in each of the AMC cases.

The use of the two CLL-deep metamaterial AMC block for antennas was also considered. Simulations of the interaction of a dipole antenna with the metamaterial block showed better than the expected AMC behavior. Resonant responses were obtained when the distance between the dipole and the metamate-
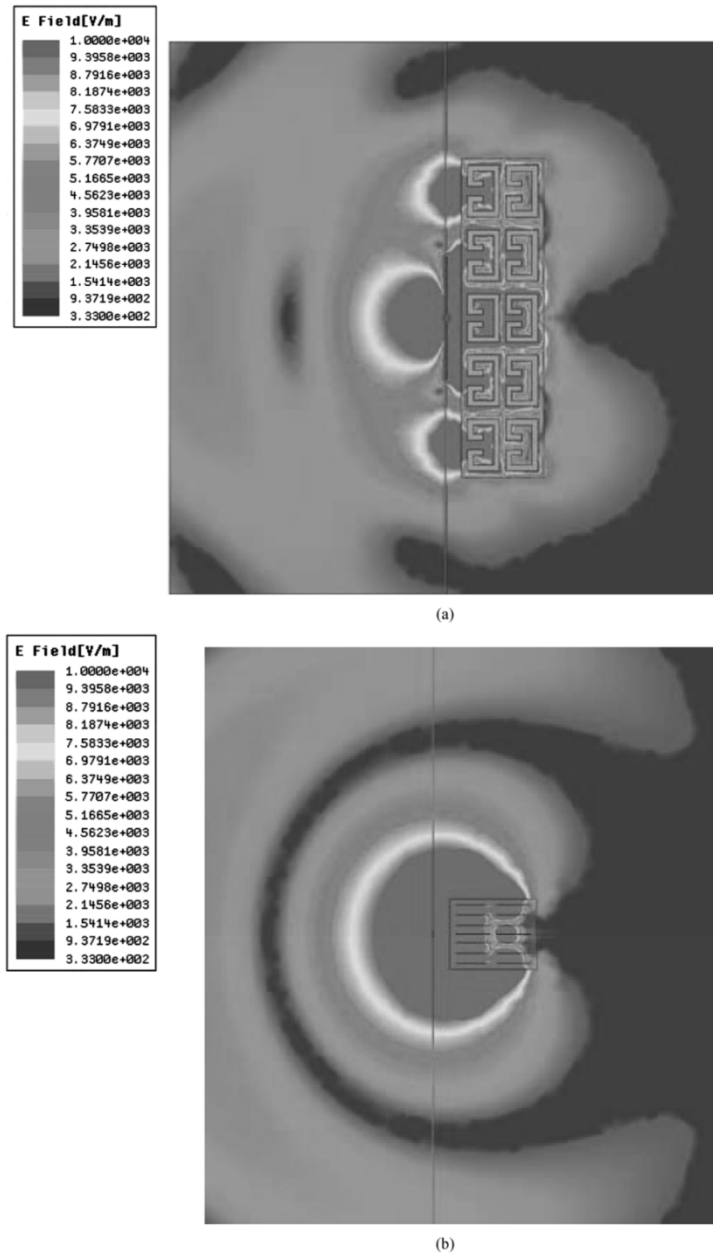
Fig. 16. HFSS predicted electric field distributions in the near field of the $0.325\lambda_0$ dipole antenna when it is in resonance with the two element CLL-based AMC block system: (a) E plane and (b) H plane.

rial block was optimized. Significantly enhanced electric field values in the reflected field region and front-to-back ratios were demonstrated.

The potential ability, for instance, of the two CLL-deep metamaterial AMC block, for instance, to shield (in the near field) a cell-phone user while more than doubling the radiated field strength away from that user (in the far field) suggests one possible application for such metamaterial-based AMC blocks. The in-phase and out-of-phase reflection properties of the CLL-based metamaterial block along with its enhanced front-to-back ratios suggests other potential wireless applications including an effective means of isolating radiating elements in close proximity to each other. Antennas other than a dipole may even be more suitable for integration with these AMC blocks. Several of these issues are being studied

currently. The results of these investigations will be reported elsewhere in the near future.

the number of elements and the original razor-blade cutting approach, there was too much variability in the final layers, hence, the overall metamaterial block. While the resulting block did show the AMC effects experimentally at 10 GHz, the results were generally quite noisy and poor. The CLL elements and the experimental protocol were completely redesigned for this latest effort. Nonetheless, Yu, Yang, and Chau's project helped lead to this successful conclusion of their initial efforts. Finally, the authors would like to thank the reviewers and the Guest Editors for their many useful suggestions.

REFERENCES

[1] D. Sievenpiper, "High-impedance electromagnetic surfaces with a forbidden frequency band," *IEEE Trans. Microw. Theory Tech.*, vol. 47, pp. 2059–2074, Nov. 1999.

[2] D. Sievenpiper, H.-P. Hsu, J. Schaffner, G. Tangonan, R. Garcia, and S. Ontiveros, "Low-profile, four-sector diversity antenna on high-impedance ground plane," *Elect. Lett.*, vol. 36, pp. 1343–1345, Aug. 2000.

[3] D. Sievenpiper, J. Schaffner, R. Loo, G. Tangonan, S. Ontiveros, and R. Harold, "A tunable impedance surface performing as a reconfigurable beam steering reflector," *IEEE Trans. Antennas Propag.*, vol. 50, no. 3, pp. 384–390, Mar. 2002.

[4] D. Sievenpiper, J. Schaffner, J.-J. Lee, and S. Livingston, "A steerable leaky-wave antenna using a tunable impedance ground plane," *IEEE Antennas Wireless Propag. Lett.*, vol. 1, pp. 179–182, 2002.

[5] F.-R. Yang, K.-P. Ma, Y. Qian, and T. Itoh, "Aperture-coupled patch antenna on uc-pbg substrate," *IEEE Trans. Microw. Theory Tech.*, vol. 47, pp. 2123–2130, Nov. 1999.

[6] R. Coccioli, F.-R. Yang, K.-P. Ma, and T. Itoh, "A novel tem waveguide using uniplanar compact photonic-bandgap (UC-PBG) structure," *IEEE Trans. Microw. Theory Tech.*, vol. 47, no. 11, pp. 2092–2098, Nov. 1999.

[7] F.-R. Yang, Y. Qian, and T. Itoh, "Antenna and circuit applications of uc-pbg structures," in *Proc. Int. Symp. Dig. on Antennas and Propagation, ISAP2000*, vol. 2, Fukuoka, Japan, Aug. 21–25, 2000, pp. 775–778.

[8] C. Caloz and T. Itoh, "A super-compact super-broadband tapered uniplanar pbg structure for microwave and milli-meter wave applications," in *Proc. IEEE MTT-S Int. Microwave Symp. Dig.*, vol. 2, Seattle, WA, Jun. 2–7, 2002, pp. 1369–1372.

[9] J. B. Pendry, A. J. Holden, D. J. Robbins, and W. J. Stewart, "Magnetism from conductors and enhanced nonlinear phenomena," *IEEE Trans. Microw. Theory Tech.*, vol. 47, pp. 2075–2084, Nov. 1999.

[10] D. R. Smith, W. J. Padilla, D. C. Vier, S. C. Nemat-Nasser, and S. Schultz, "Composite medium with simultaneously negative permeability and permittivity," *Phys. Rev. Lett.*, vol. 84, pp. 4184–4187, May 2000.

[11] R. A. Shelby, D. R. Smith, and S. Schultz, "Experimental verification of a negative refractive index of refraction," *Science*, vol. 292, pp. 77–79, Apr. 2001.

[12] R. W. Ziolkowski, "Design, fabrication, and testing of double negative metamaterials," *IEEE Trans. Antennas Propag.*, vol. 51, pp. 1516–1529, Jul. 2003.

[13] C. R. Simovski, M. Kondratiev, and S. He, "Array of C-shaped wire elements for the reduction of reflection from a conducting plane," *Microwave Opt. Tech. Lett.*, vol. 25, pp. 302–307, Jun. 2000.

[14] C.-Y. Cheng and R. W. Ziolkowski, "Tailoring double negative metamaterial reponses to achieve anomalous propagation effects along microstrip transmission lines," in *2003 IEEE MTT-S Int. Symp. Dig.*, vol. 1, Philadelphia, PA, Jun. 8–13, 2003, p. Paper TU-2C-5.

[15] A. Li and Y. Rahmat-Samii, "PBG, PMC, and PEC surface for antenna applications: A comparative study," in *Proc. IEEE AP-S Int. Symp. Dig.*, vol. 2, Salt Lake City, UT, Jul. 16–21, 2000, pp. 674–677.

[16] F. Yang and Y. Rahmat-Samii, "In-phase reflection and em wave suppression characteristics of electromagnetic band gap ground planes," in *Proc. IEEE AP-S Int. Symp. Dig.*, vol. 3, San Antonio, TX, Jun. 16–21, 2002, pp. 744–747.

[17] A. Aminia, F. Yang, and Y. Rahmat-Samii, "In-phase reflection and em wave suppression characteristics of electromagnetic band gap ground planes," in *Proc. IEEE AP-S Int. Symp. Dig.*, vol. 4, Columbus, OH, Jun. 22–27, 2003. Paper 138.1.

[18] R. Marqés, F. Medina, and R. Rafii-El-Idrissi, "Role of bianisotropy in negative permeability and left-handed metamaterials," *Phys. Rev. B*, vol. 65, p. 144 440, Apr. 2002.

[19] R. W. Ziolkowski and C.-Y. Cheng, "Existence and design of transvacuum-speed metamaterials," *Phys. Rev. E*, vol. 68, p. 026 612, Aug. 2003.

[20] R. W. Ziolkowski and F. Auzanneau, "Artificial molecule realization of a magnetic wall," *J. Appl. Phys.*, vol. 82, pp. 3192–3194, Oct. 1997.

[21] R. E. Collin and F. J. Zucker, *Antenna Theory*. New York: McGraw-Hill, 1969, p. 211.

[22] R. W. Ziolkowski, "Metamaterial realizations of perfect magnetic conductors and their applications," in *Proc. USNC/URSI Nat. Radio Science Meeting Dig.*, vol. 1, San Antonio, TX, Jun. 16–21, 2002, p. 222.

Aycan Erentok (S'02) received the B.S. (*cum laude* and honors) and M.S. degrees from the University of Arizona,Tucson, in 2001 and 2003, respectively, all in electrical engineering, where he is currently working toward the Ph.D. degree in the Electrical and Computer Engineering Department.

His research interests include genetic algorithms, conformal antennas, and the effects of metamaterials on the performance of antennas.

Mr. Erentok received third place in the student paper competition at the 2004 URSI National Radio Science Meeting in Boulder, CO.

Paul L. Luljak (S'03) received the B.S. degree in electrical engineering from the University of Arizona, Tucson, in 2004.

From 2002 to 2004, he was an Undergraduate Research Assistant with the University of Arizona, where he investigated several aspects of metamaterials, including simulations, fabrication, and measurements of artificial magnetic conductors and planar lumped element realizations. He is currently employed by the Boeing Company, St. Louis, MO.

Richard W. Ziolkowski (M'97–SM'91–F'94) received the Sc.B. degree in physics (*magna cum laude*) with honors from Brown University, Providence, RI, in 1974 and the M.S. and Ph.D. degrees in physics from the University of Illinois at Urbana-Champaign, in 1975 and 1980, respectively.

He was a member of the Engineering Research Division, Lawrence Livermore National Laboratory, CA, from 1981 to 1990, and served as the leader of the Computational Electronics and Electromagnetics Thrust Area for the Engineering Directorate, from 1984 to 1990. He joined the Department of Electrical and Computer Engineering, University of Arizona, Tuscon, as an Associate Professor in 1990, and was promoted to Full Professor in 1996. His research interests include the application of new mathematical and numerical methods to linear and nonlinear problems dealing with the interaction of acoustic and electromagnetic waves with realistic materials and structures. He was a Co-Guest Editor of the 1998 Special Issue of the *Journal of the Optical Society of America A* featuring mathematics and modeling in modern optics.

Prof. Ziolkowski is a Member of Tau Beta Pi, Sigma Xi, Phi Kappa Phi, the American Physical Society, the Optical Society of America, the Acoustical Society of America, and Commissions B (Fields and Waves) and D (Electronics and Photonics) of URSI (International Union of Radio Science). He was awarded the Tau Beta Pi Professor of the Year Award in 1993 and the IEEE and Eta Kappa Nu Outstanding Teaching Award in 1993 and 1998. He was an Associate Editor for the IEEE TRANSACTIONS ON ANTENNAS AND PROPAGATION from 1993 to 1998. He served as the Vice Chairman of the 1989 IEEE/AP-S and URSI Symposium in San Jose, and as the Technical Program Chairperson for the 1998 IEEE Conference on Electromagnetic Field Computation in Tucson. He served as a member of the IEEE AP-S Administrative Committee (ADCOM) from 2000 to 2002. He is currently serving as the IEEE AP-S Vice President/President-Elect. He was Co-Guest Editor for the October 2003 IEEE TRANSACTIONS ON ANTENNAS AND PROPAGATION Special Issue on Metamaterials. For the US URSI Society, he served as Secretary for Commission B (Fields and Waves) from 1993 to 1996 and as Chairperson of the Technical Activities Committee from 1997 to 1999, and as Secretary for Commission D (Electronics and Photonics) from 2001 to 2002. He is currently serving as a Member-at-Large of the U.S. National Committee (USNC) of URSI and is now serving as a member of the International Commission B Technical Activities Board. He was a Co-Organizer of the Photonics Nanostructures Special Symposia at the 1998, 1999, and 2000 OSA Integrated Photonics Research (IPR) Topical Meetings. He served as the Chair of the IPR subcommittee IV, Nanostructure Photonics, in 2001. He was a Steering Committee Member for the 27th ESA Antenna Technology Workshop on Innovative Periodic Antennas: Electromagnetic Bandgap, Left-handed Materials, Fractal and Frequency Selective Surfaces in Santiago de Compostela, Spain, in March 2004.